Czettl Julian

Partial-Wave and Phase-Shift Analysis of the Continuum $q\bar{q} \to ZZ \to 4\ell$ Background

Bachelor's Thesis

in partial fulfillment of the requirements for the degree of
Bachelor of Science - BSc
in Physics

submitted to
University of Graz
Graz University of Technology

Supervisor
Univ.-Prof. Dipl.-Phys. Dr.rer.nat. Axel Maas
Co-Supervisor
Dipl.-Phys. Dr.rer.nat. Simon Plaetzer

Institute of Physics

Graz, December 2025

Contents

1 Introduction

The discovery of the Higgs boson at the Large Hadron Collider (LHC) marked a major milestone in particle physics and provided decisive experimental confirmation of the mechanism responsible for the electroweak symmetry breaking and therefore the origin of the masses of the electroweak gauge bosons. After the Higgs discovery, the interest naturally shifted toward its interaction with the electroweak gauge bosons, making electroweak processes the center of many analyses. Among these, the production of ZZ pairs in proton-proton collisions emerged as particularly valuable because the resulting four-lepton final state can be reconstructed with remarkable precision and excellent kinematic resolution, which encodes detailed information about the structure of the underlying scattering amplitudes, including their angular distributions.

These angular dependencies are described by partial-wave expansion. In the case of azimuthal symmetry, which applies in this thesis, the scattering amplitude can be expressed in Legendre polynomials with complex coefficients. Reconstructing these coefficients from simulated or experimental data provides a way to probe the underlying dynamics beyond simple shape comparisons and enables access to amplitude-level information.

This thesis focuses on analyzing the angular distribution of the $pp \to ZZ \to 4\ell$ process through the polar angle θ of one Z boson in the ZZ center-of-mass frame. The distribution is expanded in a Legendre basis and the corresponding complex partial-wave amplitudes are obtained via pseudo-experiments and non-linear fitting.

The simulated data used in this thesis was produced with the Herwig 7 framework, where only the dominant continuum subprocess $q\bar{q} \to ZZ$ is simulated, while the loop-induced Higgs contributions are omitted. Because of this limitation, this thesis should be seen as a proof-of-concept study of whether partial-wave methods can extract amplitude and phase information from a finite simulated sample and whether the approach is stable enough to be used in more complete future analyses.

2 Theoretical Foundations

2.1 The Standard Model

The Standard Model (SM) of particle physics is a gauge theory and describes the strong force with quantum chromodynamics and the weak and electromagnetic forces via the unified electroweak force [1]. The SM can be described by the product group

$$SU(3)_C \times SU(2)_L \times U(1)_Y$$

where the strong interaction is described by $SU(3)_C$ and the electroweak interactions by the $SU(2)_L \times U(1)_Y$ sector.

Gluons are the gauge bosons of the strong force and therefore the $SU(3)_C$ group, they are already physical particles, whereas the gauge bosons of the electroweak force W^1, W^2 and W^3 of the $SU(2)_L$ group and B of the $U(1)_Y$ group are not. They combine into the photon γ, the neutral Z and the charged $W^\pm$. In addition to the gauge bosons mediating these forces, the SM also contains the fundamental fermions. These are arranged in three generations of quarks and three generations of leptons, which differ by their masses and quantum numbers.

2.2 Higgs Mechanism

In a pure gauge theory, gauge bosons are massless but the Z and $W^\pm$ bosons are found to be massive particles. This is explained with the Higgs mechanism [1] which introduces a scalar doublet with two complex components, governed by a Mexican hat potential

$$V(H) = -\mu^2|H|^2 + \lambda|H|^4,$$

which leads to a nonzero vacuum expectation value (VEV) that breaks the $SU(2)_L \times U(1)_Y$ symmetry of the electroweak force down to the subgroup $U(1)_{EM}$ since the charge operator

$$Q = T_3 + \tfrac{1}{2}Y$$

leaves the VEV invariant. Therefore the photon, the gauge boson of the electric charge and the unbroken subgroup $U(1)_{EM}$, stays massless, while the $W^\pm$ and Z bosons acquire mass through their interaction with the VEV.

When a continuous symmetry is spontaneously broken, massless scalar Goldstone bosons appear. Since the Higgs field has two complex components there are four real degrees of freedom. The three angular directions correspond to three Goldstone bosons, which become longitudinal components of the $W^\pm$ and Z bosons, whereas the radial fluctuation corresponds to a massive scalar particle, the Higgs.

After symmetry breaking the Higgs field can be written as fluctuation around the VEV:

$$\mathrm{H(x)}=\frac{1}{\sqrt{2}}\begin{pmatrix}0\\ v+h(x)\end{pmatrix}$$

where $v \approx 246$ GeV is the VEV and $h(x)$ the physical Higgs boson.

The fluctuation term $h(x)$ generates a coupling between the Higgs boson and a pair of W or Z bosons. Thus, information about the Higgs boson can be extracted from processes involving W and Z pairs.

2.3 Scattering

Interactions between fundamental particles can be studied through scattering processes. When two particles collide they may exchange momentum and quantum numbers, resulting in a set of final-state particles. The underlying interaction is described by the scattering amplitude $\mathcal{M}$, while experimentally accessible quantities are cross sections. The differential cross section is in general given by

$$\frac{d\sigma}{d\Omega} = \frac{1}{64\pi^2 s}\frac{|\vec{p}_f|}{|\vec{p}_i|}\,|\mathcal{M}|^2,$$

where s is the center-of-mass energy squared and $\vec{p}_{i,f}$ denote the initial- and final-state three-momenta. Since this thesis focuses on angular distributions, the angle-independent prefactor can be omitted, leaving

$$\tfrac{d\sigma}{d\Omega} \propto |\mathcal{M}|^2,$$

which describes the angular distribution of the outgoing particles.

2.4 Feynman diagrams and off-shell particles

Those scattering processes can be represented by Feynman diagrams, as shown in Fig. 1. External lines correspond to physical initial- and final-state particles, while internal lines represent intermediate propagators, which in general do not need to satisfy the classical mass-shell relation $E^2 = p^2 + m^2$ of real particles. If their squared invariant mass differs from their physical pole mass, they are said to be off-shell (virtual) particles. Such particles cannot be observed directly, but their presence can be inferred from distortions in measurable distributions like the differential cross section (see Sec. 2.6 and Eq. 1).

2.5 Subprocesses in $pp \to ZZ \to 4\ell$

The Higgs couplings to electroweak gauge bosons, as discussed in Sec. 2.2, enable decay channels that can be probed in proton-proton collisions. Of special interest is the $pp \to ZZ \to 4\ell$ channel. This channel inherits the contributions from three subprocesses:

- quark-antiquark annihilation $q\bar{q} \to ZZ \to 4\ell$
- gluon fusion via Higgs $gg \to H^* \to ZZ \to 4\ell$
- gluon fusion via quark-box diagrams $gg \to ZZ \to 4\ell$

Representative Feynman diagrams for these processes are shown in Fig. 1. Together they define the leading SM contributions to the four-lepton final state: a Higgs-mediated signal, an interfering gluon-induced background from box diagrams and a non-interfering irreducible background from the quark-antiquark annihilation, due to different initial states [2].

In this thesis, the 4ℓ final state was implemented as $e^+e^-\mu^+\mu^-$. This choice avoids same-flavor ambiguities and provides a fully reconstructible four-lepton final state with excellent mass resolution and a small, smooth background, making it ideally suited for precision studies. For this reason, the channel $H \to ZZ \to 4\ell$ is often referred to as the *golden channel* of Higgs physics [3].

Whereas in the on-shell region close to the Higgs pole $m_{ZZ} \simeq 125$ GeV the interference between the gluon-induced subprocesses is negligible due to the dominance of the Higgs resonance [4], in the off-shell region $m_{ZZ} \gg 125$ GeV the Higgs-mediated and continuum amplitudes are of comparable size, giving rise to sizeable destructive interference effects [5] thereby modifying the kinematic distribution of the final states, in particular its angular distribution. Since this thesis is conceived as a proof-of-concept study, only the continuum background subprocess $q\bar{q} \to ZZ \to 4\ell$ is simulated. This restriction is justified because the relative contribution of the gluon-induced subprocesses would be small compared to the statistical uncertainties of the limited event sample used in this study.

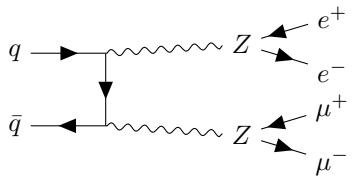

(a) Continuum background: $q\bar{q} \to ZZ$.

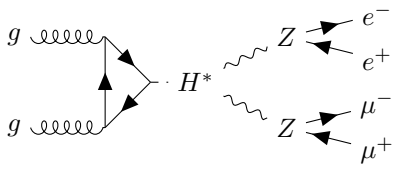

(b) Higgs signal: $gg \to H^* \to ZZ$.

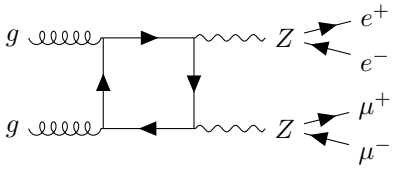

(c) Gluon–fusion background: $gg \to ZZ$.

Figure 1: Representative Feynman diagrams contributing to $pp \to ZZ \to e^+e^-\mu^+\mu^-$.

2.6 Angular variables and Lorentz boost

The kinematics of the four-lepton final states can be fully described by eight independent variables, typically chosen as the two dilepton invariant masses $m_{\mu^+\mu^-}$, $m_{e^+e^-}$ together with six angular variables describing the angular distribution. These angles consist of the polar and azimuthal orientation (θ^*, ϕ^*) of one Z boson in the ZZ center-of-mass (CM) frame, as well as the polar and azimuthal angles (θ_1, ϕ_1) and (θ_2, ϕ_2) of the decay leptons in their respective Z boson CM frame [6].
In this thesis, only a single polar angle is analyzed: the angle θ^* of one Z boson with respect to the beam axis in the ZZ CM frame. Since the two Z bosons are produced back-to-back in this frame, the angle of the second Z boson does not provide independent information and can therefore be omitted. The angle is defined in the range $0 \leq \theta \leq \pi$, with the interval $0 \leq \theta < \frac{\pi}{2}$ corresponding to the forward hemisphere and $\frac{\pi}{2} < \theta \leq \pi$ to the backward hemisphere. In case of forward-backward symmetry, which applies in this thesis, the angular distribution can be folded into the forward hemisphere without loss of information.
In experimental analyses this angle, as well as the invariant mass of the ZZ system m_{ZZ}, would be reconstructed from the momenta of the dilepton decay products. In the present simulation, however, both quantities can be accessed directly at the Z-boson level.
To evaluate the polar angle θ^* the system is boosted into the ZZ CM frame by applying a Lorentz transformation along the momentum of the ZZ system, $\vec{p}_{ZZ}$, thereby bringing the two Z bosons into the back-to-back configuration. The corresponding boost velocity is $\vec{\beta} = \frac{\vec{p}_{ZZ}}{E_{ZZ}}$ with Lorentz factor $\gamma = \frac{1}{\sqrt{1-|\vec{\beta}|^2}}$.
This transformation removes the overall momentum of the ZZ system while preserving invariant quantities such as its mass which now equals the overall energy of the system $m_{ZZ} = \sqrt{s} = E_{ZZ}$. This provides a well-defined frame in which to measure the polar angle θ^* relative to the beam axis.

A purely scalar Higgs boson would produce an isotropic θ^* distribution in the ZZ CM frame, whereas the continuum background generates richer angular structures. When both contributions are present, their interference does not simply add the two shapes but introduces additional angular information, leading to characteristic distortions such as forward-backward asymmetries.
This additional information from the angular structure arises from the interference of the $gg \to ZZ$ amplitudes in the cross section. The total amplitude for $gg \to ZZ$ is the sum of the Higgs-mediated signal contribution $\mathcal{M}_S$ and the continuum background $\mathcal{M}_B$. The observable differential cross section is proportional to the squared modulus of this total amplitude.

$$\frac{d\sigma}{d\Omega} \propto |\mathcal{M}|^2 = |\mathcal{M}_S + \mathcal{M}_B|^2 = |\mathcal{M}_S|^2 + |\mathcal{M}_B|^2 + 2\ \mathrm{Re}(\mathcal{M}_S \mathcal{M}_B^*) \qquad (1)$$

[7]. Here, the first two terms correspond purely to the signal and the background rates, while the third term represents the interference between them. This interference term modifies the angular distribution and thus provides access to additional information on the Higgs boson couplings.

2.7 Partial wave expansion and Legendre polynomials

Angular dependencies in scattering amplitudes can be described by partial waves [8]. Therefore the amplitude is expanded in spherical harmonics,

$$\mathcal{M}(\theta,\phi) = \sum_{\ell=0}^{\infty} \sum_{m=-\ell}^{\ell} a_{\ell m}\, Y_{\ell m}(\theta,\phi),$$

where the complex coefficient $a_{\ell m}$ is the partial-wave amplitude and corresponds to the contribution of each angular momentum mode. For azimuthal symmetric processes only $m = 0$ contributes and the spherical harmonic reduces to

$$Y_{\ell 0}(\theta,\phi) = \sqrt{\frac{2\ell+1}{4\pi}}\, P_\ell(\cos\theta).$$

When used to express the amplitude, the normalization gets absorbed by the definition of the partial-wave coefficient a_ℓ and the amplitude can be written as

$$\mathcal{M}(\cos\theta) = \sum_{\ell=0}^{\infty} (2\ell+1)\, a_\ell\, P_\ell(\cos\theta).$$

The Legendre polynomials $P_\ell(\cos\theta)$ form a complete orthogonal basis on the interval $-1 \leq \cos\theta \leq 1$

$$\int_{-1}^{1} P_\ell(x)\, P_{\ell'}(x)\, dx = \frac{2}{2\ell+1}\, \delta_{\ell\ell'},$$

Describing the observable differential cross section leads naturally into a double sum over products of Legendre polynomials

$$\frac{d\sigma}{d\Omega} \;\propto\; \left|\mathcal{M}(\cos\theta)\right|^2 \;=\; \sum_{\ell} \sum_{\ell'} (2\ell+1)(2\ell'+1)\, a_\ell a_{\ell'}^*\, P_\ell(\cos\theta)\, P_{\ell'}(\cos\theta) \qquad (2)$$

which can be re-expressed as a single Legendre series by means of addition theorems,

$$P_\ell(\cos\theta)\, P_{\ell'}(\cos\theta) \;=\; \sum_{L=0}^{\ell+\ell'} C_{\ell\ell' L}\, P_L(\cos\theta), \qquad (3)$$

so that

$$\frac{d\sigma}{d\Omega} \;\propto\; \sum_{L=0}^{\infty} b_L\, P_L(\cos\theta), \qquad b_L \;=\; \sum_{\ell,\ell'} (2\ell+1)(2\ell'+1)\, a_\ell a_{\ell'}^*\, C_{\ell\ell' L}. \qquad (4)$$

In practice, the coefficients b_L can be obtained by fitting the angular distribution from simulated events to a Legendre series. From these coefficients, the partial-wave amplitudes a_ℓ can be reconstructed by solving the corresponding

system of equations. In this thesis, however, the partial-wave amplitudes are extracted by fitting them to discrete evaluation points of the Legendre expansion $\sum_{L=0}^{N} b_L \; P_L(\cos\theta)$ obtained in the first step. This indirect approach introduces an additional source of uncertainty, since the partial-wave amplitudes are no longer fitted directly to the data. In addition, the limited event statistics can lead to fluctuations that obscure higher-order terms and destabilize the phase reconstruction.

As b_L is a derived quantity the underlying physical information still resides in the complex partial wave-amplitude a_ℓ.

Since the angular distribution in this thesis is forward-backward symmetric and can be folded as discussed in Sec. 2.6, this symmetry

$$\frac{d\sigma}{d\Omega}(\cos\theta) = \frac{d\sigma}{d\Omega}(-\cos\theta),$$

and the fact that Legendre polynomials obey

$$P_\ell(-x) = (-1)^\ell P_\ell(x)$$

leads to the elimination of all odd partial waves, so that $a_\ell = 0$ for odd ℓ. This is consistent with the physical interpretation: the isotropic s-wave corresponding to $\ell = 0$ remains as the leading contribution, while the p-wave corresponding to $\ell = 1$, which would generate forward-backward asymmetry, vanishes.

The partial-wave amplitude a_ℓ can also be expressed in polar form as

$$a_\ell = r_\ell e^{i\phi_\ell}$$

where r_ℓ corresponds to the magnitude of the partial wave amplitude and ϕ_ℓ represents the phase.

2.8 Phase shifts

The phases ϕ_ℓ represent the relative phase shifts between the different partial waves and therefore quantify how much the outgoing waves are delayed or advanced with respect to free propagation due to the interaction. While the absolute phases δ_ℓ are not directly observable, their relative differences $\Delta\phi_{\ell m}$ are, which encode physical information about the interference of different angular momentum contributions.

3 Simulation & Data Analysis Methods

3.1 Event Generation

The simulated data used in this thesis were generated with HERWIG 7.2.2 [9–46]

event generator, a general-purpose Monte Carlo generator for high-energy collisions. It combines matrix element calculations with parton-shower evolution and non-perturbative models.

Event generation employed the Matchbox framework with the `LHC-Matchbox.in` template. This template is configured for proton-proton collisions for LHC conditions, with appropriate beam setup and PDF handling.

Collisions were simulated at a center-of-mass energy of $\sqrt{s} = 13$ TeV for the process $pp \to e^+e^-\ \mu^+\mu^-$. Matrix elements were provided through the MADGRAPH–OPENLOOPS interface. The calculation was performed at leading order in the electroweak coupling ($\mathcal{O}(\alpha_{\mathrm{EW}}^4)$) with no QCD corrections ($\mathcal{O}(\alpha_s^0)$), thus including only the $q\bar{q}$-initiated channel. The loop-induced $gg \to ZZ$ contribution and interference were not considered here as stated earlier. Parton distribution functions were taken from the CT14 set in the five-flavor scheme. The **lepton-pair mass scale** was used as a dynamical choice for the factorization and renormalization scales. Events were showered using the MC@LO default shower setup. Both dilepton pairs were required to satisfy $60 < m_{\ell\ell} < 120$ GeV (via `ChargedLeptonPairMassCut`) to select Z-boson candidates. The full input file used for this setup is provided in App. D.1.

A total of 10000 events were generated with no explicit random seed set and saved in `HepMC` format.

3.2 Rivet Analysis

The generated events were then analyzed using the RIVET framework, based on a modified version of the the standard `MC_ZZINC` analysis.

The two `ZFinder`s for e^+e^- and $\mu^+\mu^-$ with their standard selection ($p_T > 25$ GeV, $|\eta| < 3.5$, $65 < m_{\ell\ell} < 115$ GeV, photon recombination $\Delta R = 0.2$) are retained. The ZZ system is reconstructed and the folded polar angle $\theta_{\mathrm{fold}} = \arccos(|\cos\theta^*|)$ of the $Z_{\mu^+\mu^-}$ candidate with respect to the beam axis is evaluated in the ZZ rest frame and filled in three m_{ZZ} intervals ([160,190], [195,225] and [230,260] GeV) with 15 bins between 0 and $\frac{\pi}{2}$. An inclusive m_{ZZ} spectrum is also produced. All histograms are normalized using the standard RIVET cross-section scaling. The histograms were saved as YODA files and converted to `.dat` tables for further post-processing. The corresponding HERWIG 7.2.2 distributions are provided in App. B, App. C. The corresponding analysis file is provided in App. D.2.

It should be noted that the lowest mass window $m_{ZZ} \in [160, 190]$ GeV lies partially below the on-shell threshold for a physical ZZ system ($2m_Z \approx 182$ GeV). While the two `ZFinder`s select dilepton pairs within $65 < m_{\ell\ell} < 115$ GeV, such that the reconstructed bosons individually satisfy the Z-window cuts, their combination does not guarantee an on-shell ZZ state.

3.3 Data post-processing and fitting

3.3.1 Data preparation

For post-processing, the `.dat` files were loaded into a Python script. The total cross section was obtained by integrating the differential distribution using a bin-wise Riemann sum $\sigma = \sum_i \frac{d\sigma}{dX}_i \Delta X_i$ and used for normalization. The angle θ for each bin was taken as the bin $\theta_i = \frac{1}{2}(x_{\text{low,i}} + x_{\text{high,i}})$. Since the statistical uncertainties are symmetric $\delta_{-,i} = \delta_{+,i}$, a single symmetric uncertainty was used in the further script as error in both directions $\delta_{\pm,i} = \delta_{-,i}$.

3.3.2 Legendre-coefficient fit

Candidate Legendre expansions $\sum_{L=0}^{N} b_L P_L(\cos\theta)$ with even degrees N (due to folding) were tested.

For each m_{ZZ} interval, the coefficients b_L were obtained by solving a weighted linear least-squares problem. The design matrix $V_{i,L} = P_L(\cos\theta_i)$ was constructed from the bin centers θ_i, and statistical uncertainties σ_i were incorporated as weights $w_i = 1/\sigma_i^2$. The coefficients minimize

$$\chi^2 = \sum_i w_i \left[y_i - \sum_{L=0}^{N} b_L P_L(\cos\theta_i)\right]^2,$$

which is equivalent to solving the normal equations $(V^{\mathrm{T}}WV)\mathbf{b} = V^{\mathrm{T}}W\mathbf{y}$. The system was solved using `numpy.linalg.solve`, with a pseudoinverse fallback for near-singular cases. The covariance matrix of the fitted coefficients is then given by $\mathbf{C}_b = (V^{\mathrm{T}}WV)^{-1}$ and will be used in Sec. 3.3.4.

Fit quality was assessed using the reduced chi-squared (χ^2_{red}) and the mean value $\bar{\chi}^2_{\text{red}}$ over all m_{ZZ} intervals for each polynomial degree N. The resulting mean values are summarized in Tab. 1.

Table 1: Average reduced chi-squared values $\bar{\chi}^2_{\text{red}}$ across the three m_{ZZ} intervals for different maximal Legendre degrees N.

N	$\bar{\chi}^2_{\text{red}}$
4	7.36
6	2.72
8	**1.74**
10	1.62

Although the lowest $\bar{\chi}^2_{\text{red}}$ occurred at $N = 10$, the corresponding fits showed signs of overfitting, as can be seen in figure 2. Therefore, $N = 8$ was chosen as the optimal compromise between goodness of fit and model stability and was used across all m_{ZZ} intervals to ensure comparability. Additional fits for all tested degrees and m_{ZZ} intervals are provided in App. A.

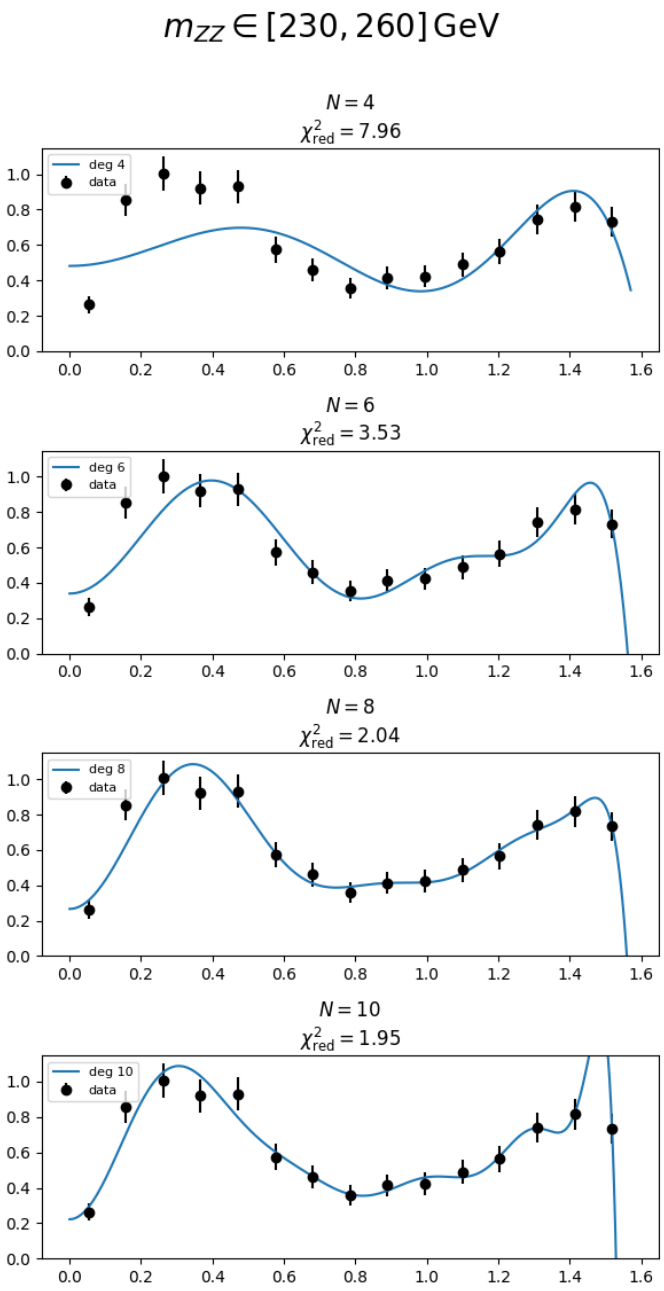

Figure 2: Legendre fits with different maximal degrees N to the angular distribution in the $m_{ZZ} \in$ [230,260] GeV interval. Reduced chi-squared values χ^2_{red} are indicated in each panel.

3.3.3 Pseudo data generation

Since $|\mathcal{M}|^2$ is modeled as a double Legendre series and fitted in terms of the coefficients b_L, uncertainties were propagated via Monte-Carlo pseudo-experiments rather than analytically. A total of 300 pseudo-experiments were performed.

For each pseudo-experiment t, a coefficient vector was drawn from a multivariate normal distribution $\mathcal{N}(\mu, \Sigma)$ with mean $\hat{\mathbf{b}}$ equal to the best-fit Legendre coefficients b_L and the covariance $\mathbf{C}_b$ given by their fitted symmetrized covariance matrix (for numerical stability),

$$\mathbf{b}^{(t)} \sim \mathcal{N}\Big(\hat{\mathbf{b}},\, \mathbf{C}_b\Big), \qquad \hat{\mathbf{b}} = (\hat{b}_0, \ldots, \hat{b}_N).$$

Each pseudo-experiment was evaluated on a grid of $K = 50$ equidistant points covering the data range $\{\theta_k\}_{k=1}^{K}$:

$$y^{(t)}(\theta_k) = \sum_{L=0}^{N} b_L^{(t)}\, P_L(\cos\theta_k)$$

3.3.4 Amplitude fit

The pseudo-experiment spectra were fitted with the amplitude model $y(\theta) \approx |\sum_{\ell=0}^{N=8} a_\ell P_\ell(\cos\theta)|^2$ as defined in Eq. 2, where the $(2\ell+1)$ terms are absorbed into the complex coefficients a_ℓ. The coefficients a_ℓ were parameterized in polar form $a_\ell = r_\ell e^{i\phi_\ell}$. To ensure comparability a maximal degree of $N = 8$ was used again in all m_{ZZ} intervals.

The fit was again performed by minimizing a weighted least-squares objective

$$\chi^2 \;=\; \sum_{k=1}^{K} w_k \big[y^{(t)}(\theta_k) - \big|\sum_{\ell=0}^{N} a_\ell P_\ell(\cos\theta_k)\big|^2\big]^2,$$

where the weights $w_k = \frac{1}{\sigma_k^2}$ and σ_k are the per-point uncertainties propagated from the Legendre-coefficient covariance $\mathbf{C}_b$ via $\mathbf{C}_y = V\,\mathbf{C}_b\,V^{\mathrm{T}}$ (diagonal approximation), such that $\sigma_k = \sqrt{(\mathbf{C}_y)_{kk}}$.

Bound constraints $r_\ell \geq 0$ and $\phi_\ell \in [-\pi, \pi]$ were imposed and the global phase was fixed ($\phi_0 = 0$). To mitigate convergence to local minima, each pseudo-experiment was fitted ten times with random initializations generated using NumPy's `default_rng` (PCG64) with a fixed seed for reproducibility, and the solution with the lowest chi-squared (χ^2) was retained.

The uncertainty band is obtained from the ensemble of fitted amplitude curves: at each angle θ the central prediction is the median over the retained pseudo-experiment curves and the shaded band shows the pointwise central 68% interval. For plotting, the curves are evaluated on a dense grid across the data range as can be seen in Fig. 3.

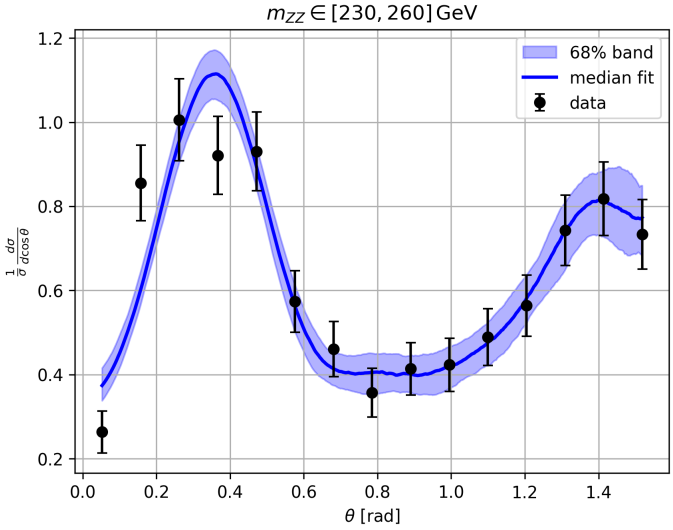

Figure 3: Fit of the amplitude model $|\sum_{\ell=0}^{8} a_\ell P_\ell(\cos\theta)|^2$ to pseudo-data in the $m_{ZZ} \in [230, 260]$ GeV interval.

3.3.5 Phase distributions

To obtain a meaningful phase shift distribution, the ϕ_s samples are filtered. Only phase samples $\phi_{s,\ell}$ associated with sufficiently large amplitudes $r_{s,\ell}$ are retained, thereby suppressing random fluctuations in regions of low amplitude. For each multipole ℓ, the median amplitude $r_{\text{med},\ell}$ is calculated and only phase values $\phi_{s,\ell}$ with corresponding amplitudes $r_{s,\ell} \geq 0.05 \cdot r_{\text{med},\ell}$ are retained.

The circular mean for each phase shift distribution is calculated and visualized in a rose plot together with the corresponding distribution of the relevant even phases. Additionally, the shortest 68% arc around the mean is indicated as can be seen in Fig. 4. The zero phase is excluded, as it is fixed to zero by definition and does not carry physical meaning.

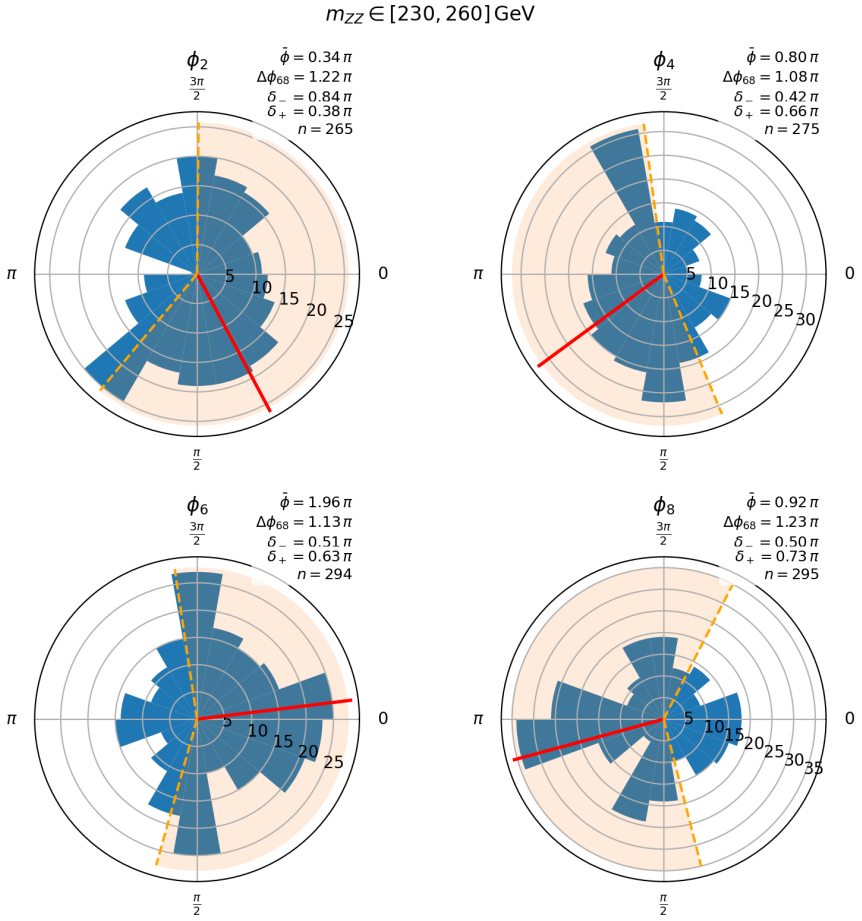

Figure 4: Phase distributions ϕ_ℓ of the complex coefficients $a_\ell = r_\ell e^{i\phi_\ell}$ obtained from the ensemble of pseudo-experiment fits in the $m_{ZZ} \in [230, 260]$ GeV interval. For each multipole, circular mean $\bar{\phi}$, central 68% interval width $\Delta\phi_{68}$, one-sided deviations $\delta_\pm$ (all expressed in units of π) and the number of retained phase samples n, are indicated.

4 Results

4.1 Angular Distributions

To study the shape evolution of the angular distribution, the raw data seen in Fig. 5 is examined alongside the normalized spectra presented in Figs. 6, 7 and 8 in the next subsection.

The raw distributions primarily illustrate the relative population of the three mass windows. As expected from the mass distribution shown in App. B, most events lie in the intermediate mass window ($m_{ZZ} \in [195, 225]$ GeV) while the higher mass window ($m_{ZZ} \in [230, 260]$ GeV) contains fewer events and the lowest mass window ($m_{ZZ} \in [160, 190]$ GeV) receives only a very small fraction of the total sample. The low population in the lowest mass window is expected because the mass window lies only partially in the on-shell ZZ region. The physical cross section is small and the off-shell configurations that populate the sub-threshold region are also rare. Therefore, the statistics in this region are strongly limited. Consequently the lowest mass window appears mostly structureless.

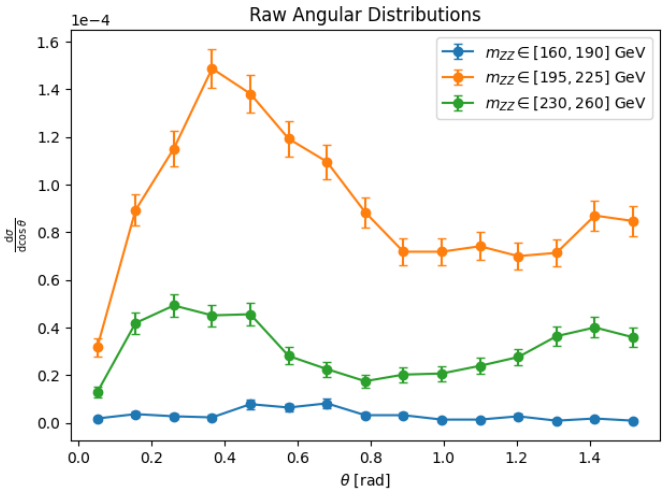

Figure 5: Raw θ distributions in the three m_{ZZ} intervals.

After normalization the lowest mass window shows a largely uniform and slightly noisy distribution that saturates quickly at small angles, with a small, broader enhancement at around 0.6 rad that introduces a modest amount of structure.

In contrast, the second and third mass windows seem to follow a continuous evolution: as the invariant mass increases, the narrow enhancement observed near 0.4 rad broadens into a wider plateau. At the same time, the lower plateau at larger angles shifts its center slightly from 1.1 rad to around 0.9 rad and the

small rise at 1.4 rad develops into a secondary, lower peak.

Since the statistical precision varies across the three mass windows, the intermediate m_{ZZ} range exhibits the smallest uncertainties after normalization, whereas the lowest mass window shows larger uncertainties.

4.2 Fitted Amplitudes and Uncertainty Bands

Although a physical interpretation of the fitted amplitudes is not possible in this setup, it can be assessed how well the method describes the angular distribution and whether the amplitude and phase extraction in the following section behave reliably.

The fitted amplitude model is compared with the normalized angular data in Figs. 6, 7 and 8. The blue curves represent the median of the fitted amplitudes, while the shaded regions indicate the 68% uncertainty bands derived from the ensemble of pseudo-experiments.

In the lowest mass window ($m_{ZZ} \in [160, 190]$ GeV), the agreement between data and fit is limited by large statistical fluctuations due to limited statistics. Only one of the three bins forming the central enhancement lies close to the median fit, while the remaining two fall outside the uncertainty band, with only parts of their negative uncertainties overlapping. The remaining points lie mostly within the band or are at least consistent within their uncertainties. The fit follows the general trend but shows oscillations at larger angles that likely arise from statistical noise and overfitting. The overall width of the band is large, reflecting the low statistics and weak angular structure in this mass region.

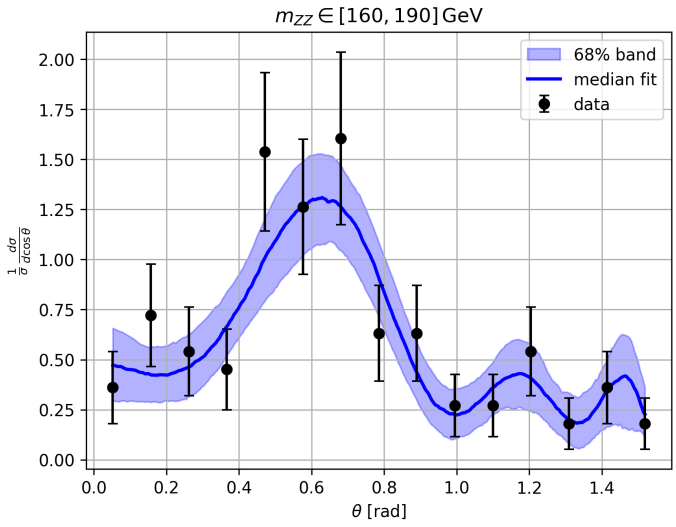

Figure 6: Normalized angular distribution for events in the mass interval $m_{ZZ} \in [160, 190]$ GeV.

The fit in the intermediate mass window ($m_{ZZ} \in [195, 225]$ GeV) describes the data considerably better, except for the first two bins, which deviate with their uncertainties from the band. Most of the other points lie within the small 68% region. The general structure with the peak, the steady decline to the lower plateau and the small rise at the end is therefore clearly visible in the fit. In this mass window, the band is narrow during the steep rise but widens at the peak and again at the plateau, roughly matching the size of the experimental errors. The overall description of the structure is good, although slight bumps during the descent to the plateau and within may indicate minor overfitting to statistical fluctuations.

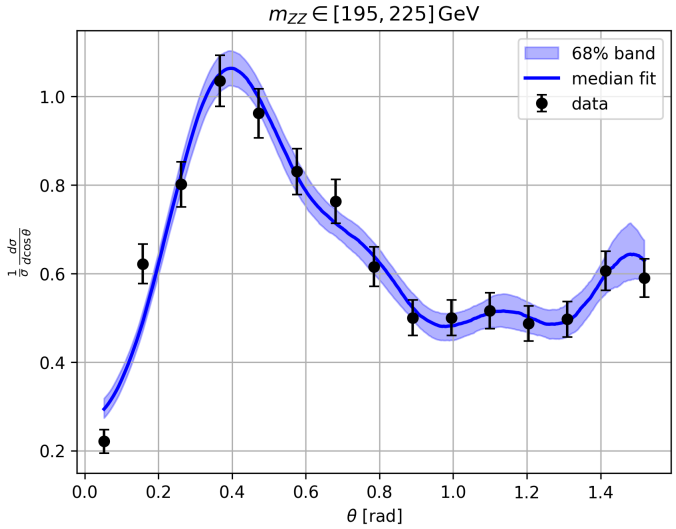

Figure 7: Normalized angular distribution for events in the mass interval $m_{ZZ} \in [195, 225]$ GeV.

In the highest mass window ($m_{ZZ} \in [230, 260]$ GeV) the first two bins again deviate with their uncertainties from the uncertainty band as well as the fourth bin at the peak. The remaining bins lie within the 68% region, many close to the median fit. The band broadens again at the peak and from the plateau onward, roughly matching the sizes of the experimental errors. The rise toward the second, smaller peak is also captured well.

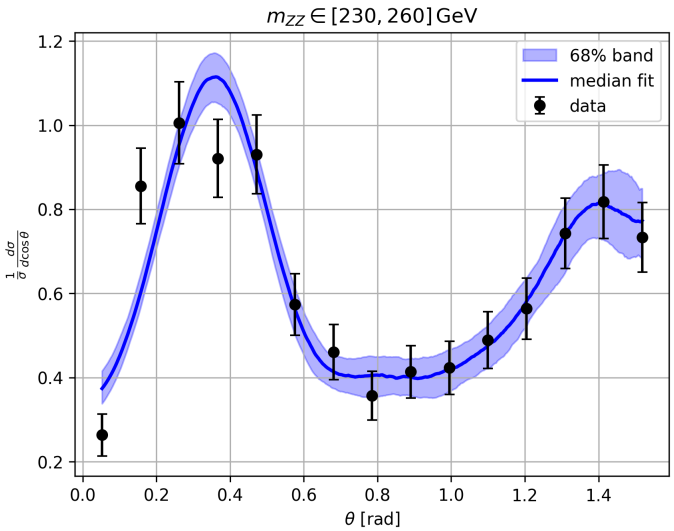

Figure 8: Normalized angular distribution for events in the mass interval $m_{ZZ} \in [230, 260]$ GeV.

Since the fits originate from Monte Carlo simulations, no χ^2 values are reported. Instead, the fit quality is assessed visually through the 68% uncertainty bands. These bands reproduce the overall shapes within statistical fluctuations, and their close correspondence to the experimental error bars in some regions indicates that the fits correctly reflect the statistical precision of the underlying data.

4.3 Phase Shift Distributions

The extracted phase shift distributions for the even ϕ values are shown in Figs. 9, 10 and 11.

In the lowest mass window ($m_{ZZ} \in [160, 190]$ GeV) the phase distributions for ϕ_6 and ϕ_8 are sharply peaked and well-aligned around 2π with very small peaks in the angle at opposing direction at π. The distribution for ϕ_4 shows a sharp well aligned peak at π. Whereas the ϕ_2 distribution shows a strong peak at 2π and a notable peak at π with some noise in other directions. This slightly bimodal shape of the ϕ_2 distribution likely originates from its higher sensitivity to small anisotropies in the angular spectrum, such as the enhancement visible

around 0.6 rad in Fig. 6. In addition, the intrinsic 2π-periodicity of the phase leads to numerically equivalent solutions separated by π, causing the peaks at opposite angles and producing the unusually broad 68% interval in the ϕ_2 rose plot. Since in nearly flat angular distributions only the lowest partial waves contribute appreciably, while higher-order waves are strongly suppressed, the distributions of ϕ_6 and ϕ_8 are likely aligned by chance. Their phases are dominated by statistical noise due to the absence of pronounced angular structure and tend to align due to numerical minimization symmetry.

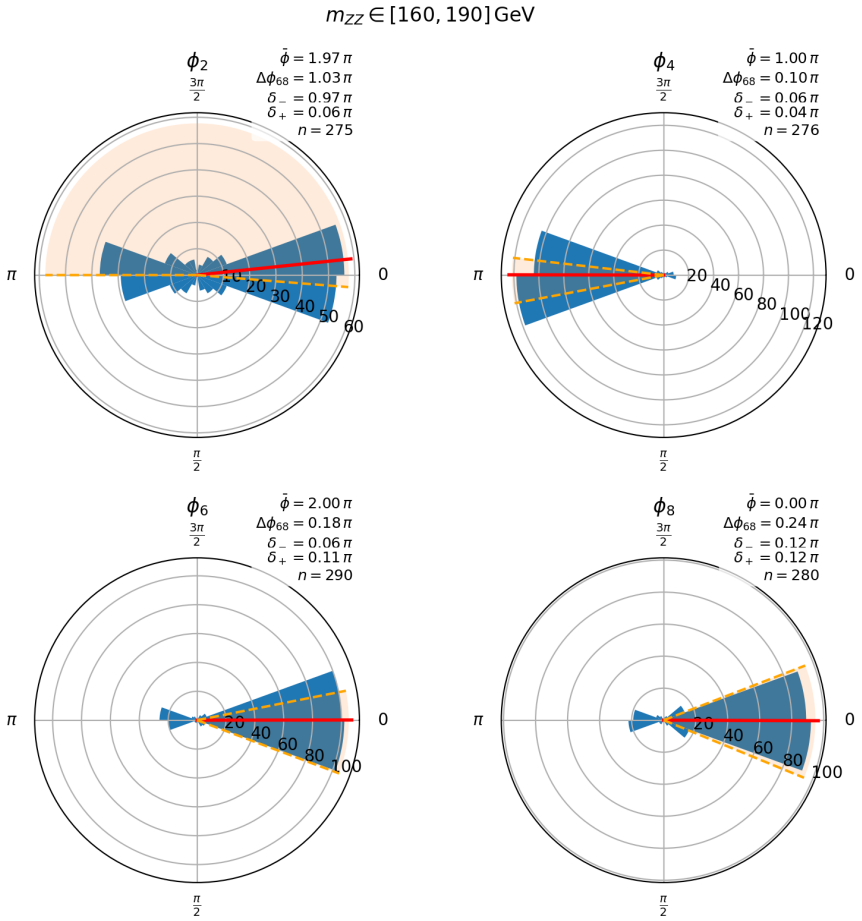

Figure 9: Phase distributions of the extracted partial-wave phases ϕ_ℓ for events in the mass interval $m_{ZZ} \in [160, 190]$ GeV. For each distribution, the circular mean $\bar{\phi}$, the width of the 68% interval $\Delta\phi_{68}$, its positive and negative deviations from the circular mean $\delta_\pm$ and the population n are indicated.

At intermediate mass range ($m_{ZZ} \in [195, 225]$ GeV), the phase distributions broaden significantly, with the 68% intervals now covering nearly half of the possible phase range for each component. All distributions still show a clear tendency to cluster around π or 2π, with noticeable lower population at the opposing direction, suggesting that partial coherence among the components is still maintained.

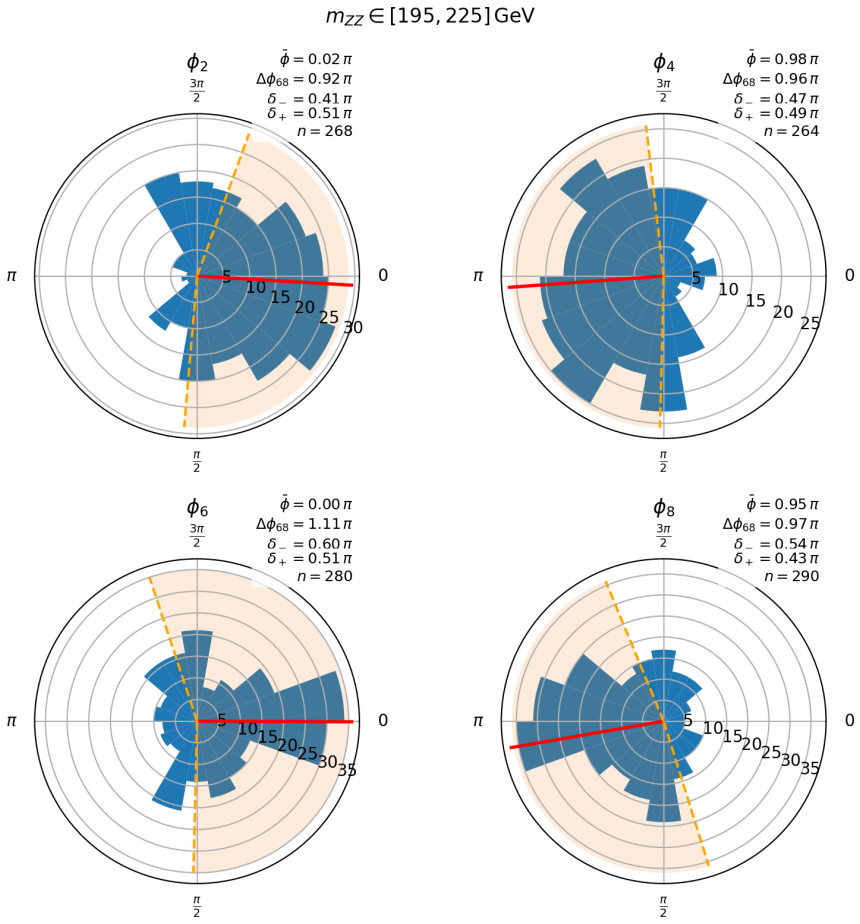

Figure 10: Phase distributions of the extracted partial-wave phases ϕ_ℓ for events in the mass interval $m_{ZZ} \in [195, 225]$ GeV. For each distribution, the circular mean $\bar{\phi}$, the width of the 68% interval $\Delta\phi_{68}$, its positive and negative deviations from the circular mean $\delta_\pm$ and the population n are indicated.

In the heavy mass range ($m_{ZZ} \in [230, 260]$ GeV), the phase distributions continue to broaden, with the 68% intervals now covering more than half of the possible phase range. Only the ϕ_6 and ϕ_8 distributions retain circular means near π and 2π, respectively While the ϕ_8 distribution shows a clear trend toward its circular mean at π, the other distributions exhibit pronounced peaks at additional phase angles besides its circular mean. This and the broadening of the 68% region from the intermediate to the highest mass window indicates a transition from a partially coherent phase structure to a regime dominated by stronger interference among multiple contributing partial waves within the fitted model.

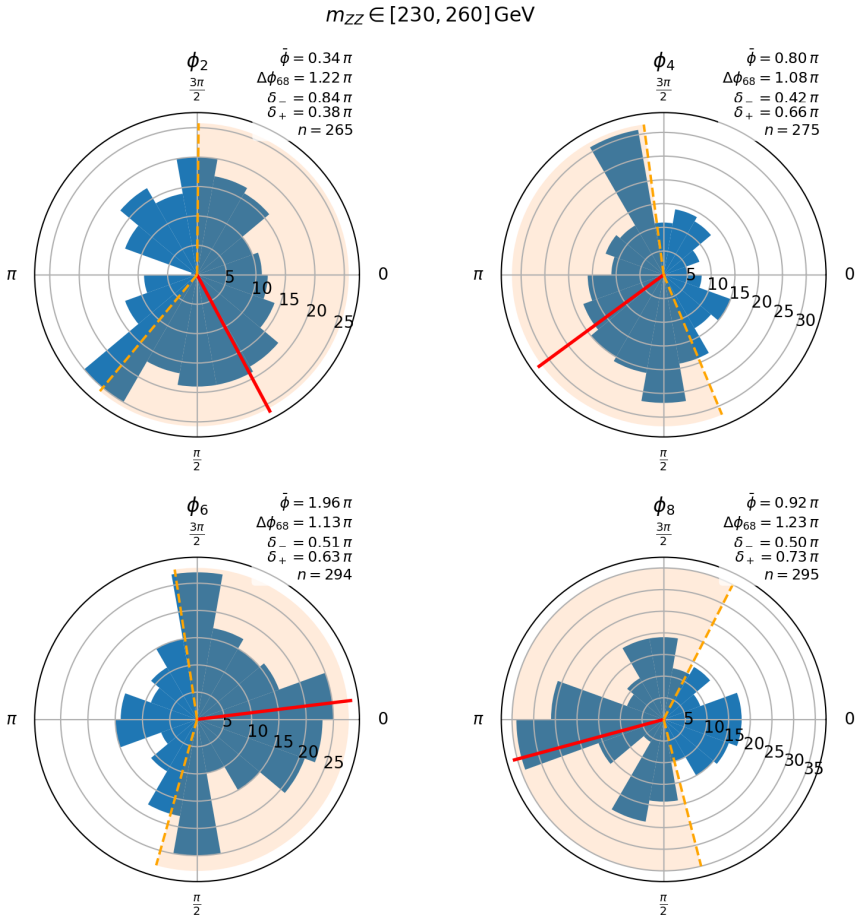

Figure 11: Phase distributions of the extracted partial-wave phases ϕ_ℓ for events in the mass interval $m_{ZZ} \in [230, 260]$ GeV. For each distribution, the circular mean $\bar{\phi}$, the width of the 68% interval $\Delta\phi_{68}$, its positive and negative deviations from the circular mean $\delta_\pm$ and the population n are indicated.

The circular means across the mass windows show an overall consistency of phase orientations with a gradual reduction in coherence at higher invariant masses. In the two lower m_{ZZ} intervals only ϕ_8 shifts from alignment at 2π in the lowest mass window to π in the intermediate one. This is consistent with the assumption that ϕ_8 does not carry any physical information in the lowest mass window and becomes partially constrained with the appearance of angular structure in the second mass window.

In the highest mass window, ϕ_2 and ϕ_4 lose their alignment and exhibit only circular mean values without dominant directions. This behavior suggests that the overall phase structure remains largely unchanged, with the onset of phase decoherence and increasing interference effects of the fitted model appearing at the highest m_{ZZ} values.

5 Conclusion

The results show that the Legendre-based amplitude parametrization is capable of describing the evolution of angular distributions with increasing m_{ZZ} and of extracting information on the associated phase shifts. While the lowest mass window is dominated by statistical fluctuations, the intermediate and highest windows exhibit clear angular modulations and a continuous evolution that are well reproduced by the fitted amplitude bands.
The phase distributions demonstrate that the phases are not uniquely determined: sharp peaks in the lowest mass window arise from fit degeneracies, while the two higher mass windows produce broader and partly multimodal solutions. This indicates that the extraction technique alone is not sufficient to provide unique or well-constrained phase solutions.

Despite these limitations, the method as a whole is sensitive to the emergence of angular structure and is therefore promising for Higgs applications once the Higgs-induced sub-processes are included and physically meaningful interference becomes accessible. However, several challenges need to be addressed before the approach can be reliably applied to real data. The amplitude-level fit shows numerical instabilities and converges to different phase configurations depending on initialization. The phase extraction itself requires stabilization through filtering, regularization or coherence criteria.

Higher statistics would further improve the determination of partial-wave contributions, particularly in the low-mass region. This could be partially achieved by balancing out the statistics over the three mass windows. By adjusting the window sizes, the sub-threshold region of the lowest mass window could be excluded and the event populations equalized, leading to more stable amplitude and phase estimates in that region.

Additionally, the forward-backward folding used in this thesis is appropriate for the symmetric continuum background but may obscure possible asymmetric interference effects between the Higgs-induced and continuum processes. Recovering the full angular range would therefore be necessary for a realistic Higgs analysis.

This proof-of-concept thesis therefore provides a first step toward a more complete phase-based analysis of Higgs-induced processes, motivating further development and application to realistic datasets.

References

[1] Michael E. Peskin and Daniel V. Schroeder. *An Introduction to Quantum Field Theory*. Addison-Wesley, 1995. ISBN: 978-0-201-50397-5.

[2] Aleksandr Azatov et al. "Taming the off-shell Higgs boson". In: *Zh. Eksp. Teor. Fiz.* 147 (2015), pp. 410–425. DOI: 10.1134/S1063776115030140. arXiv: 1406.6338 [hep-ph].

[3] Hua-Rong He, Xia Wan, and You-Kai Wang. "Anomalous $H \to ZZ \to 4\ell$ decay and its interference effects on gluon–gluon contribution at the LHC". In: *Chin. Phys. C* 44.12 (2020), p. 123101. DOI: 10.1088/1674-1137/abb4c8. arXiv: 1902.04756 [hep-ph].

[4] Fabrizio Caola and Kirill Melnikov. "Constraining the Higgs boson width with ZZ production at the LHC". In: *Phys. Rev. D* 88 (2013), p. 054024. DOI: 10.1103/PhysRevD.88.054024. arXiv: 1307.4935 [hep-ph].

[5] Nikolas Kauer and Giampiero Passarino. "Inadequacy of zero-width approximation for a light Higgs boson signal". In: *JHEP* 08 (2012), p. 116. DOI: 10.1007/JHEP08(2012)116. arXiv: 1206.4803 [hep-ph].

[6] Yi-Song Lu, You-Kai Wang, and Xiang-Yuan You. "Study of HZZ anomalous couplings by angular differential cross sections". In: (Nov. 2022). arXiv: 2211.07478 [hep-ph].

[7] Giampiero Passarino. "Higgs Interference Effects in $gg \to ZZ$ and their Uncertainty". In: *JHEP* 08 (2012), p. 146. DOI: 10.1007/JHEP08(2012)146. arXiv: 1206.3824 [hep-ph].

[8] R. G. Newton. *Scattering Theory of Waves and Particles*. 1982.

[9] L. Lönnblad. "ThePEG". In: *Comput. Phys. Commun.* 118 (1999), p. 213.

[10] M. Bahr et al. "Herwig Physics and Manual". In: *Eur. Phys. J. C* 58 (2008), p. 639. arXiv: 0803.0883 [hep-ph].

[11] G. Marchesini and B. R. Webber. "Simulation Of QCD Jets Including Soft Gluon Interference". In: *Nucl. Phys. B* 238 (1984), p. 1.

[12] G. Marchesini and B. R. Webber. "Monte Carlo Simulation of General Hard Processes with Coherent QCD Radiation". In: *Nucl. Phys. B* 310 (1988), p. 461.

[13] S. Gieseke, P. Stephens, and B. Webber. "New formalism for QCD parton showers". In: *JHEP* 0312 (2003), p. 045. eprint: hep-ph/0310083.

[14] B. R. Webber. "A QCD Model For Jet Fragmentation Including Soft Gluon Interference". In: *Nucl. Phys. B* 238 (1984), p. 492.

[15] P. Richardson. "Spin correlations in Monte Carlo simulations". In: *JHEP* 0111 (2001), p. 029. eprint: hep-ph/0110108.

[16] J. Alwall et al. "MadGraph 5: Going Beyond". In: (2011). arXiv: 1106.0522 [hep-ph].

[17] S. Platzer and S. Gieseke. "Dipole Showers and Automated NLO Matching in Herwig". In: (2011). arXiv: 1109.6256 [hep-ph].

[18] Herwig Collaboration. "Precision LHC Event Generation with Herwig". In: (2015). In preparation.

[19] M. Sjödahl. "ColorFull: a C++ library for calculations in SU(Nc) color space". In: (2014). arXiv: 1412.3967 [hep-ph].

[20] S. M. Flatte. "Coupled-Channel Analysis Near K Kbar Threshold". In: *Phys. Lett. B* 63 (1976), p. 224.

[21] M. Q. Huang et al. In: *Phys. Lett. B* 502 (2001), p. 133. eprint: hep-ph/0012114.

[22] R. L. Singleton. "Semileptonic baryon decays with a heavy quark". In: *Phys. Rev. D* 43 (1991), p. 2939.

[23] M. A. Ivanov et al. "Heavy baryon transitions in a relativistic three-quark model". In: *Phys. Rev. D* 56 (1997), p. 348. eprint: hep-ph/9612463.

[24] A. Kupco. "Cluster hadronization in HERWIG 5.9". In: (1999). eprint: hep-ph/9906412.

[25] F. Schlumpf. In: *Phys. Rev. D* 51 (1995), p. 2262. eprint: hep-ph/9409272.

[26] M. Bahr, S. Gieseke, and M. Seymour. "Simulation of multiple partonic interactions in Herwig". In: *JHEP* 0807 (2008), p. 076. eprint: 0803.3633.

[27] M. Bahr et al. "Soft interactions in Herwig". In: (2009). eprint: 0905.4671.

[28] J. H. Kuhn and A. Santamaria. "Tau decays to pions". In: *Z. Phys. C* 48 (1990), p. 445.

[29] G. Gounaris and J. Sakurai. "Finite width corrections to the vector meson dominance prediction". In: *Phys. Rev. Lett.* 21 (1968), p. 244.

[30] D. Asner et al. In: *Phys. Rev. D* 61 (2000), p. 012002. eprint: hep-ex/9902022.

[31] H. Y. Cheng and B. Tseng. In: *Phys. Rev. D* 53 (1996), p. 1457. eprint: hep-ph/9502391.

[32] H. Y. Cheng. In: *Phys. Rev. D* 56 (1997), p. 2799. eprint: hep-ph/9612223.

[33] G. Corcella et al. "HERWIG 6.5". In: *JHEP* 0101 (2001), p. 010. eprint: hep-ph/0011363.

[34] B. Borasoy and B. Holstein. In: *Phys. Rev. D* 60 (1999), p. 054021. eprint: hep-ph/9905398.

[35] R. Kleiss and W. Stirling. In: *Nucl. Phys. B* 385 (1992), p. 413.

[36] A. Aloisio et al. In: *Phys. Lett. B* 561 (2003), p. 55. eprint: hep-ex/0303016.

[37] N. Beisert and B. Borasoy. In: *Nucl. Phys. A* 716 (2003), p. 186. eprint: hep-ph/0301058.

[38] M. Gormley et al. In: *Phys. Rev. D* 2 (1970), p. 501.

[39] W. Tippens et al. In: *Phys. Rev. Lett.* 87 (2001), p. 192001.

[40] E. P. Venugopal and B. Holstein. In: *Phys. Rev. D* 57 (1998), p. 4397. eprint: hep-ph/9710382.

[41] B. Holstein. In: *Phys. Scripta* T99 (2002), p. 55. eprint: hep-ph/0112150.

[42] J. Korner and M. Kramer. In: *Z. Phys. C* 55 (1992), p. 659.

[43] B. Borasoy and B. Holstein. In: *Phys. Rev. D* 59 (1999), p. 094025. eprint: hep-ph/9902351.

[44] M. A. Ivanov et al. In: *Phys. Rev. D* 60 (1999), p. 094002. eprint: hep-ph/9904421.

[45] M. A. Ivanov, J. Korner, and V. E. Lyubovitskij. In: *Phys. Lett. B* 448 (1999), p. 143. eprint: hep-ph/9811370.

[46] B. Borasoy and B. Holstein. In: *Phys. Rev. D* 59 (1999), p. 054019. eprint: hep-ph/9902431.

6 Appendix

A Legendre-coefficient fit

For completeness, the full set of Legendre coefficient fits performed for all tested maximal degrees $N = 4, 6, 8, 10$ in each of the three m_{ZZ} intervals to complement the discussion in Sec. 3.3.2 and illustrate how the behavior changes with increasing polynomial order.

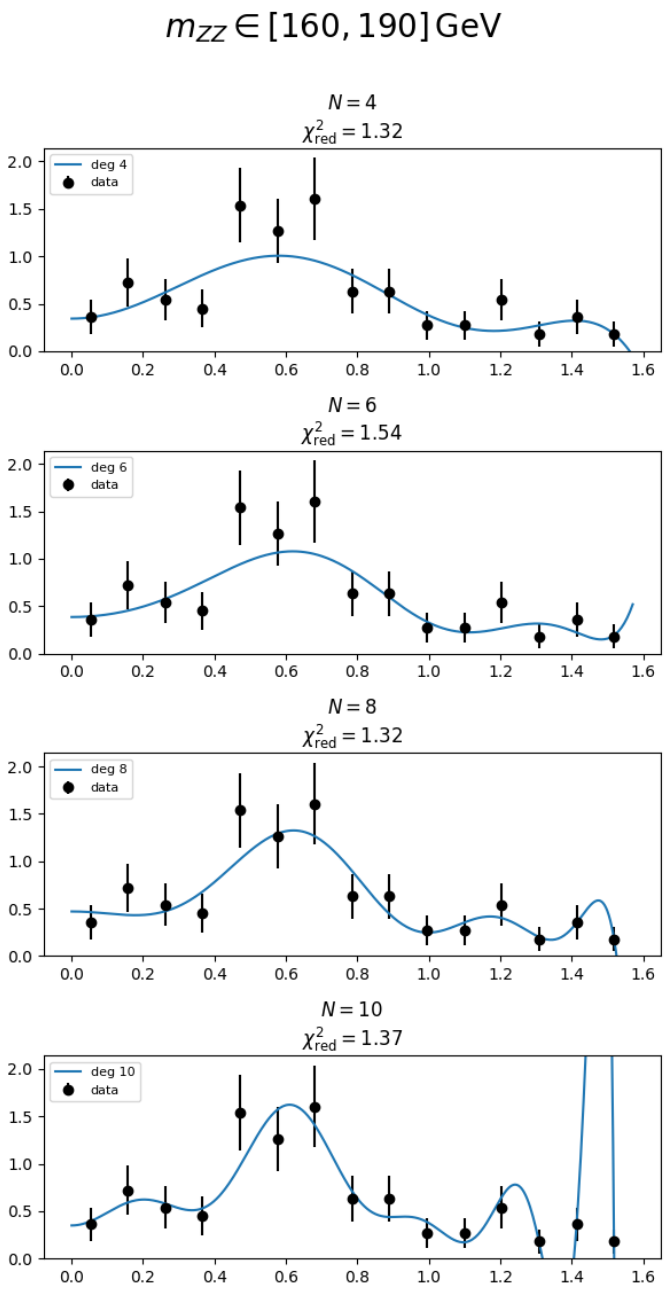

Figure 12: Legendre fits with different maximal degrees N in the low-mass interval $m_{ZZ} \in [160, 190]$ GeV. Reduced chi-squared values χ^2_{red} are indicated in each panel.

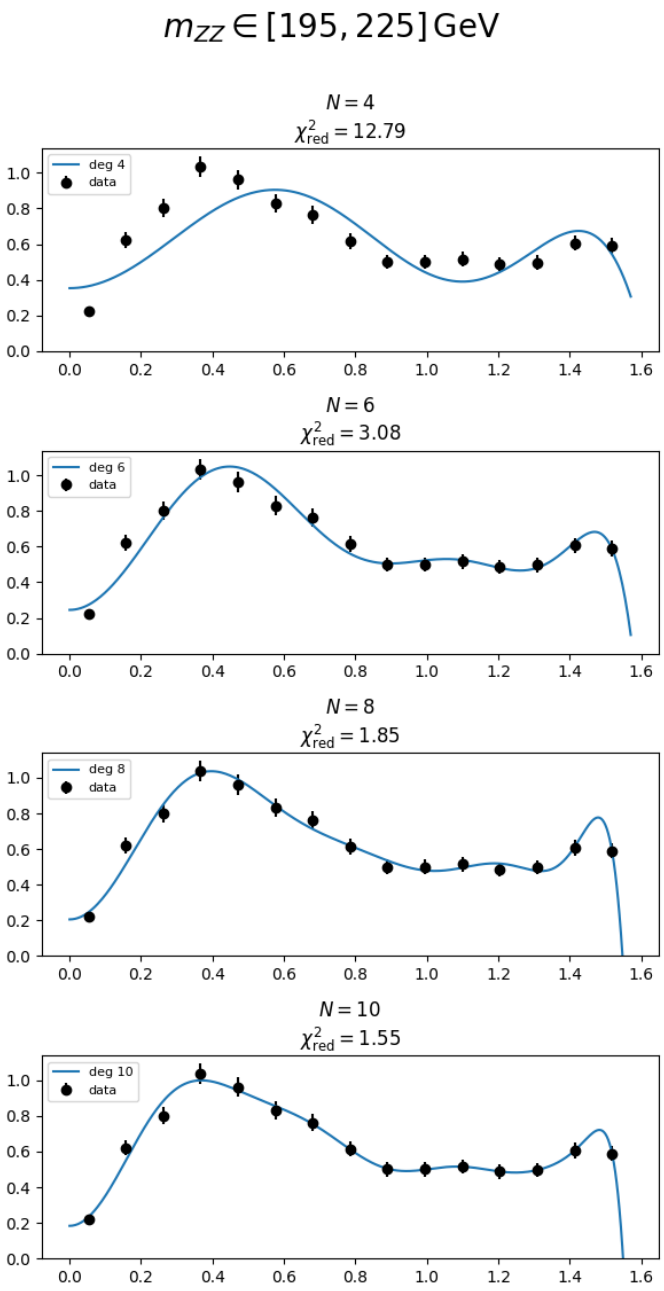

Figure 13: Legendre fits with different maximal degrees N in the mid-mass interval $m_{ZZ} \in [195, 225]$ GeV. Reduced chi-squared values χ^2_{red} are indicated in each panel.

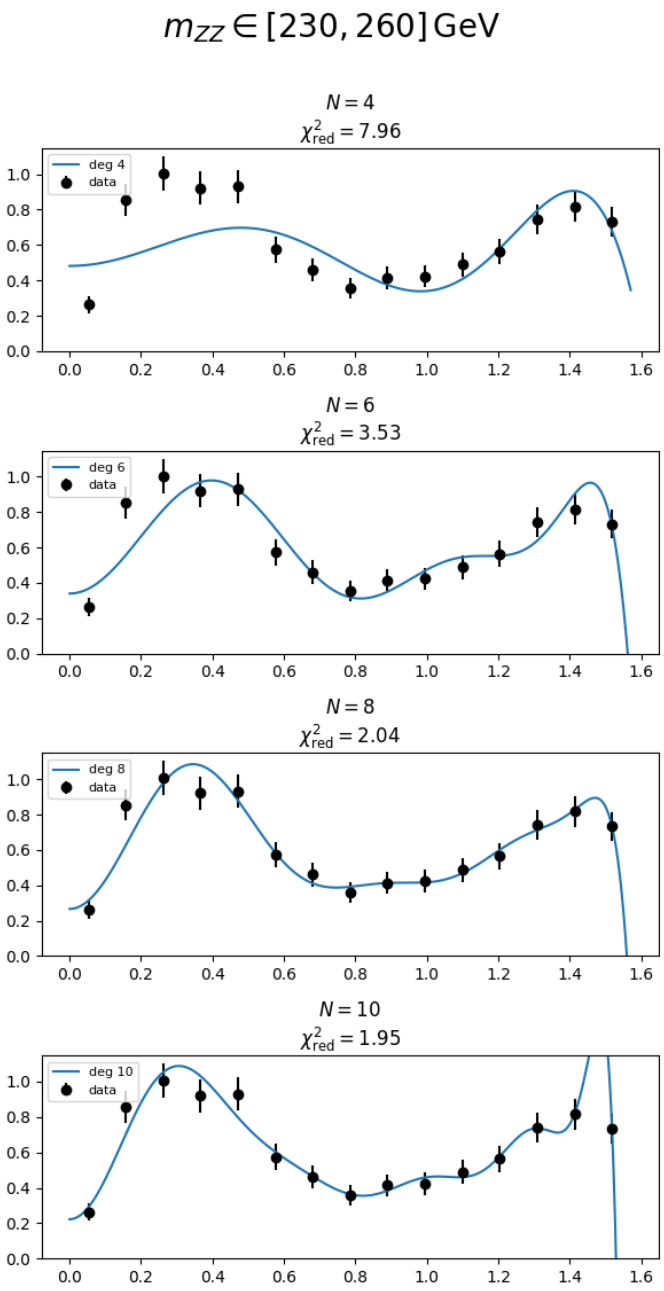

Figure 14: Legendre fits with different maximal degrees N in the high-mass interval $m_{ZZ} \in [230, 260]$ GeV. Reduced chi-squared values χ^2_{red} are indicated in each panel.

B Invariant Mass Distribution m_{ZZ}

The distribution below shows the invariant mass spectrum of the simulated ZZ system containing one $Z \to e^+e^-$ and one $Z \to \mu^+\mu^-$ decay. The histogram is normalized to the generator cross section using the total number of weighted events.

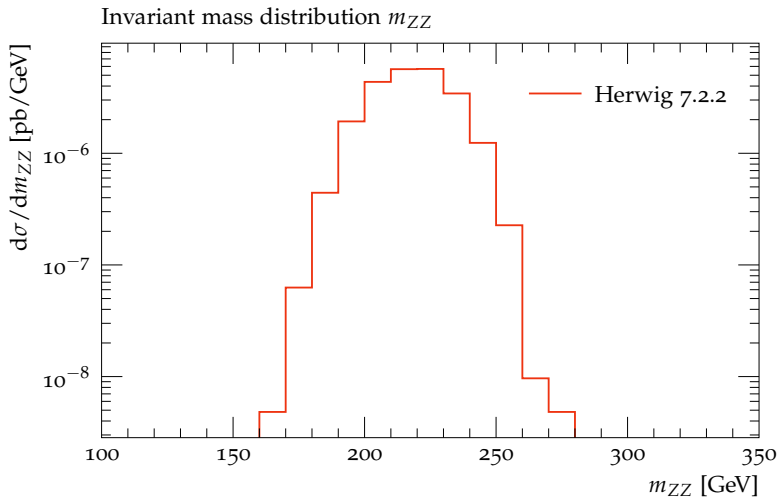

Figure 15: Invariant mass distribution of the reconstructed ZZ system in HERWIG 7.2.2 simulated events.

C Angular Distributions $\theta_{Z\to\mu\mu}$

The following figures show the production angle $\theta_{Z\to\mu\mu}$ of the $Z \to \mu^+\mu^-$ boson, defined as the angle between the $Z \to \mu\mu$ momentum and the incoming beam direction in the ZZ centre-of-mass frame. The observable is folded to $\theta \in [0, \frac{\pi}{2}]$ and normalized to the generator cross section.

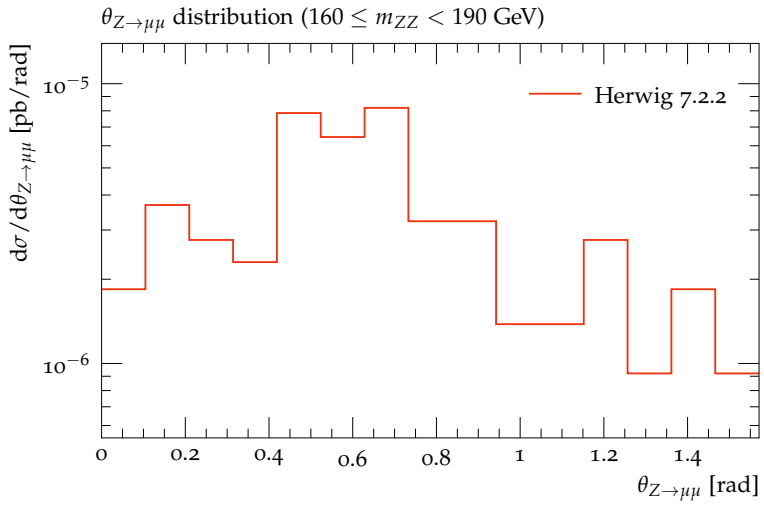

Figure 16: Folded production angle $\theta_{Z\to\mu\mu}$ in the $160 \leq m_{ZZ} < 190$ GeV range, simulated using the continuum background $q\bar{q} \to ZZ$ process in Herwig 7.2.2. The $Z \to \mu\mu$ boson is reconstructed in the ZZ rest frame and the angle is measured with respect to the beam direction.

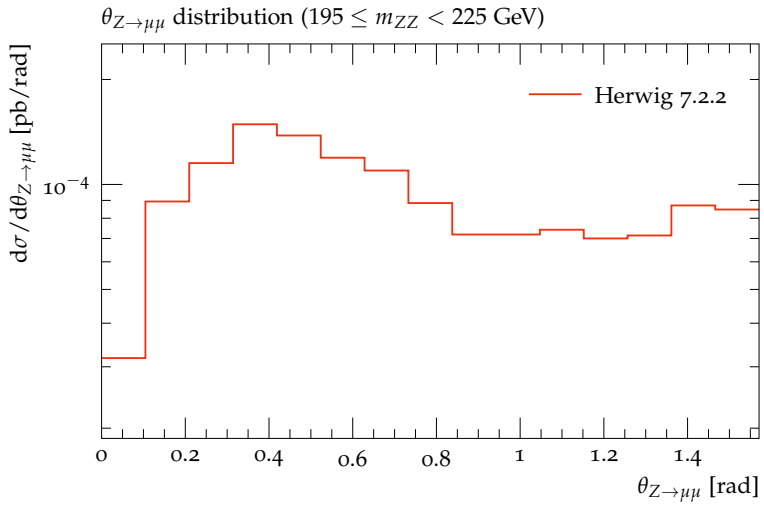

Figure 17: Folded production angle $\theta_{Z\to\mu\mu}$ in the $195 \leq m_{ZZ} < 225$ GeV range, simulated using the continuum background $q\bar{q} \to ZZ$ process in HERWIG 7.2.2. The $Z \to \mu\mu$ boson is reconstructed in the ZZ rest frame and the angle is measured with respect to the beam direction.

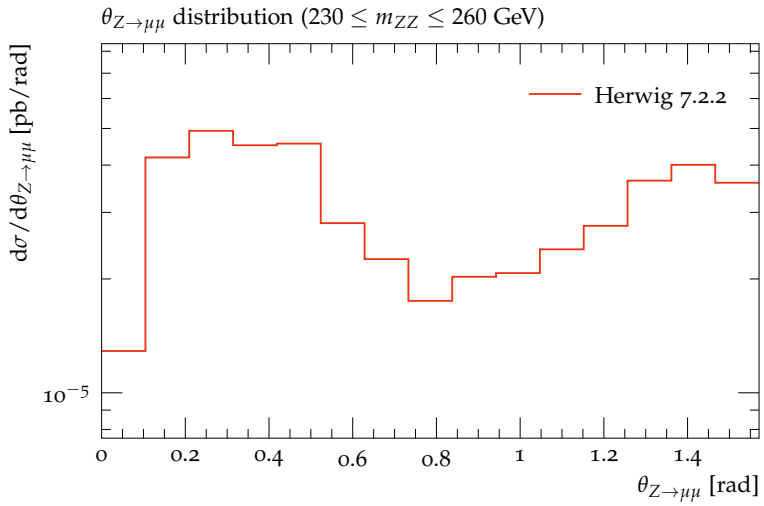

Figure 18: Folded production angle $\theta_{Z\to\mu\mu}$ in the $230 \leq m_{ZZ} \leq 260$ GeV range, simulated using the continuum background $q\bar{q} \to ZZ$ process in HERWIG 7.2.2. The $Z \to \mu\mu$ boson is reconstructed in the ZZ rest frame and the angle is measured with respect to the beam direction.

D Herwig Files

D.1 LHC-Matchbox.in

```
# -*- ThePEG-repository -*-

##################################################
## Herwig/Matchbox input
##################################################

##################################################
## Collider type
##################################################
read snippets/Matchbox.in
read snippets/PPCollider.in

##################################################
## Beam energy √s = 13 TeV
##################################################
cd /Herwig/EventHandlers
set EventHandler:LuminosityFunction:Energy 13000*GeV

##################################################
## Model assumptions
##################################################
read Matchbox/StandardModelLike.in
read Matchbox/DiagonalCKM.in

##################################################
## Process definition (inclusive 4l)
##################################################
cd /Herwig/MatrixElements/Matchbox
set Factory:OrderInAlphaS 0
set Factory:OrderInAlphaEW 4
do Factory:Process p p -> e+ e- mu+ mu-

##################################################
## Matrix element library
##################################################
read Matchbox/MadGraph-OpenLoops.in

##################################################
## Cuts on lepton pairs
##################################################
cd /Herwig/Cuts
set ChargedLeptonPairMassCut:MinMass 60*GeV
set ChargedLeptonPairMassCut:MaxMass 120*GeV

##################################################
```

```
## Scale choice
######################################################
cd /Herwig/MatrixElements/Matchbox
set Factory:ScaleChoice /Herwig/MatrixElements/Matchbox/Scales/
    LeptonPairMassScale

######################################################
## Shower setup (LO)
######################################################
read Matchbox/MCatLO-DefaultShower.in

######################################################
## PDF
######################################################
read Matchbox/FiveFlavourScheme.in
read Matchbox/CT14.in

######################################################
## Analyses (Rivet)
######################################################
cd /Herwig/Analysis
insert Rivet:Analyses 0 MC_ZZANG
insert /Herwig/Generators/EventGenerator:AnalysisHandlers 0
    Rivet

######################################################
## Build run and save
######################################################
do /Herwig/MatrixElements/Matchbox/Factory:ProductionMode

cd /Herwig/Generators
saverun LHC-Matchbox EventGenerator
```

D.2 MC_ZZANG.cc

```
// -*- C++ -*-
#include "Rivet/Analysis.hh"
#include "Rivet/Projections/ZFinder.hh"
#include "Rivet/Projections/VetoedFinalState.hh"

namespace Rivet {


  /// @brief Rivet analysis computing the folded polar angle of
       Z[mumu] in Z[ee]Z[mumu] events
  class MC_ZZANG : public Analysis {
  public:

    /// Default constructor
    MC_ZZANG()
      : Analysis("MC_ZZANG")
    {    }


    /// @name Analysis methods
    //@{

    /// Book histograms
    void init() {

      Cut cut = Cuts::abseta < 3.5 && Cuts::pT > 25*GeV;
      ZFinder zeefinder(FinalState(), cut, PID::ELECTRON, 65*
          GeV, 115*GeV,
                        0.2, ZFinder::ClusterPhotons::NODECAY,
                            ZFinder::AddPhotons::YES);
      declare(zeefinder, "ZeeFinder");

      VetoedFinalState zmminput;
      zmminput.addVetoOnThisFinalState(zeefinder);
      ZFinder zmmfinder(zmminput, cut, PID::MUON, 65*GeV, 115*
          GeV,
                        0.2, ZFinder::ClusterPhotons::NODECAY,
                            ZFinder::AddPhotons::YES);
      declare(zmmfinder, "ZmmFinder");

      book(_h_thetaZZ_m160_190, "thetaZZ_m160_190", 15, 0.0, PI
          /2);
      book(_h_thetaZZ_m195_225, "thetaZZ_m195_225", 15, 0.0, PI
          /2);
      book(_h_thetaZZ_m230_260, "thetaZZ_m230_260", 15, 0.0, PI
          /2);
      book(_h_mZZ, "mZZ", 25, 100.0, 350.0);
    }
```

```
/// Do the analysis
void analyze(const Event& e) {


  const ZFinder& zeefinder = apply<ZFinder>(e, "ZeeFinder")
      ;
  if (zeefinder.bosons().size() != 1) vetoEvent;
  const ZFinder& zmmfinder = apply<ZFinder>(e, "ZmmFinder")
      ;
  if (zmmfinder.bosons().size() != 1) vetoEvent;



  // Z momenta
  const FourMomentum& zee = zeefinder.bosons()[0].momentum
      ();
  const FourMomentum& zmm = zmmfinder.bosons()[0].momentum
      ();
  const FourMomentum zz = zee + zmm;

  const double mZZ = zz.mass()/GeV;

  const double weight = 1.0;




  // Boost zee and zmm to the ZZ rest frame
  LorentzTransform boost_to_ZZ_rest = LorentzTransform::
      mkFrameTransformFromBeta(zz.betaVec());
  FourMomentum boosted_zee = boost_to_ZZ_rest.transform(zee
      );
  FourMomentum boosted_zmm = boost_to_ZZ_rest.transform(zmm
      );

  const Vector3 nhat_mm  = boosted_zmm.p3().unit();
  const double  costh_mm = nhat_mm.z();

  // fold: |cos(theta)| in [0,1]  ->  theta in [0, pi/2]
  const double  u_fold      = std::fabs(costh_mm);
  const double  theta_fold  = std::acos(u_fold);

  double thetaZmm = theta_fold;

  _h_mZZ->fill(mZZ, weight);

  if (mZZ >= 160.0 && mZZ < 190.0) {
  _h_thetaZZ_m160_190->fill(thetaZmm, weight);
  } else if (mZZ >= 195.0 && mZZ < 225.0) {
```

```
      _h_thetaZZ_m195_225->fill(thetaZmm, weight);
      } else if (mZZ >= 230.0 && mZZ <= 260.0) {
      _h_thetaZZ_m230_260->fill(thetaZmm, weight);
      } else {
       return;
      }


    }


    /// Finalize
    void finalize() {
      const double s = crossSection()/picobarn/sumOfWeights();
      scale(_h_thetaZZ_m160_190, s);
      scale(_h_thetaZZ_m195_225, s);
      scale(_h_thetaZZ_m230_260, s);
      scale(_h_mZZ, s);
    }

  private:
    /// @name Histograms
    Histo1DPtr _h_thetaZZ_m160_190;
    Histo1DPtr _h_thetaZZ_m195_225;
    Histo1DPtr _h_thetaZZ_m230_260;
    Histo1DPtr _h_mZZ;
    //@}

  };

  // The hook for the plugin system
  RIVET_DECLARE_PLUGIN(MC_ZZANG);

}
```